Journal of Materials Chemistry A, Volume 7, Issue 16, April 2019, pp. 9977-9987
DOI: 10.1039/C8TA10472G

# Fundamental studies of carbon capture using CaO-based materials

Hongman Sun,[ab] Jianqiao Wang,[c] Xiaotong Liu,[b] Boxiong Shen,*[c] Christopher M. A. Parlett,*[d] George O. Adwek,[c]

Edward J. Anthony,*[e] Paul T. Williams*[f] and Chunfei Wu*[abc]

[a] *School of Chemistry and Chemical Engineering, Queen's University Belfast, Belfast BT7 1NN, UK*

[b] *School of Engineering and Computer Science, University of Hull, Hull HU6 7RX, UK*

[c] *School of Energy and Environmental Engineering, Hebei University of Technology, Tianjin 300401, China*

[d] *School of Chemical Engineering and Analytical Science, University of Manchester, Manchester M1 3AL, UK*

[e] *Centre for Combustion and CCS, Cranfield University, Cranfield MK43 0AL, UK*

[f] *School of Chemical and Process Engineering, University of Leeds, Leeds LS2 9JT, UK*

**Abstract:** Detailed understanding of the mechanisms of the fast stage during CaO carbonation is important to the design of novel efficient CaO materials. This work systematically studies the formation of $CaCO_3$ product layer on the outside surface of CaO grains during the fast reaction stage for carbon capture using two types of CaO adsorbents. The carbonation at 400 ˚C filled the small pores in the commercial CaO grains and no distinct product layer of $CaCO_3$ was observed. However, a distinct layer of $CaCO_3$ with a thickness around 90 nm was observed on the outside surface of the commercial CaO grains after the carbonation at 600 ˚C because the internal pores in the CaO grain had been filled and a layer of $CaCO_3$ product was deposited on the outside surface of the CaO grain. For sol-gel CaO, the carbonation reaction is limited by the availability of useful porosity for the growth of $CaCO_3$ product (confinement effect), instead of by the diffusion of ions in the critical layer of the $CaCO_3$ product. No surface product layer was observed. Therefore, fabricating nano-CaO having dimensions less than the critical thickness of the $CaCO_3$ layer (~90 nm) is of potentially great significance if it can be done cheaply and in bulk.

*Corresponding authors:

E-mail: c.wu@qub.ac.uk (C. Wu); p.t.williams@leeds.ac.uk (P.T. Williams), b.j.anthony@cranfield.ac.uk (E.J. Anthony); christopher.parlett@manchester.ac.uk (C. Parlett); shenbx@hebut.edu.cn (B. Shen).

## 1. Introduction

Greenhouse gas especially $CO_2$ emissions are responsible for climate change and the reduction of greenhouse gas is important to the sustainable development of modern society.[1] It has been reported by the Intergovernmental Panel on Climate Change (IPCC) that the global risks of climate change are increasingly clear for agriculture, human health, ecosystems, and water supplies. The IPCC concluded in 2014 that the world was ill-prepared for such risks.[2] Subsequently, the Parties to the United Nations Framework Convention on Climate Change (UNFCCC) reached a landmark agreement (the Paris Agreement) to accelerate actions and increase investments towards a sustainable and low-carbon future.[3] Carbon capture and utilisation (CCU) have been attracting increasing attention.[4, 5] $CO_2$ absorption using amine solution is commercially available. However, as noted by Haszeldine et al. [6] and Sadiq et al.,[7] an estimated 30% of power plant output is required for the regeneration of sorbents for carbon capture from post-combustion flue gas, because heating water in the amine sorbent causes large energy losses. On the other hand, using solid sorbents to capture $CO_2$ is attractive, with the following advantages: (1) the lower heat capacity of solids significantly reduces the sensible energy required for sorbent regeneration; (2) corrosion problems caused by the use of amine solutions (the current standard carbon capture method) are avoided;[8] (3) heat released during the exothermic carbon capture reaction at a high operating temperature (comparable to gas turbine exhaust temperature)[9] can be extracted by steam for power generation enabling a highly efficient steam cycle. CaO, as one of the high-temperature $CO_2$ sorbents, has been investigated extensively because of its high reactivity for $CO_2$ capture and high theoretical uptake capacity of 17.8 mmol $g^{-1}$, as well as the extensive availability of CaO precursors possessing a low-cost nature.[10-14] One 1 MWth long-term pilot testing facility and a 1.7 MWth CaL pilot were constructed in Technische Universität Darmstadt and La Pereda power plant, respectively.[15, 16] It

was found that the semi-industrial CaL plants achieved an outstanding $CO_2$ capture efficiency (>90%) with a good operation stability (1200 h). In addition, a 1.9 MWth pilot plant constructed at 2013 in Taiwan confirmed that the CaL process is a promising technology for $CO_2$ capture.[17] However, one of the main limitations of CaO derived from natural precursors is the sorbent deactivation during the regeneration process due to the sintering of CaO particles at high regeneration temperature.[18-20] This behaviour can be explained by considering the dramatic volume change between CaO and CaO to $CaCO_3$; for example an increase from 16.7 to 36.9 $cm^3$ $mol^{-1}$ for CaO to $CaCO_3$. Furthermore, there are two stages in the carbonation reaction of CaO: an initially fast reaction stage and a subsequently slow reaction stage.[21-23] It is attributed that the reduction of carbonation rate in the slow stage was caused by the $CO_2$ diffusion through the formed $CaCO_3$ product.[22] In the carbonation process, the ratio of reaction rates between the fast and slow reaction stages was around 100.[24] This value is in good consistency with the ratio of diffusion coefficients for CaO (0.3 $cm^2$ $s^{-1}$) and $CaCO_3$ (0.003 $cm^2$ $s^{-1}$).[22, 25] Therefore, Barker suggested that there was a critical $CaCO_3$ product layer at which the carbonation reaction rate was determined by the $CO_2$ diffusion.[22] During the fast reaction stage, $CaCO_3$ grew on the surface of CaO grains and then collapsed to form a continuous layer on the outside surface of the unreacted adsorbent. Thereafter, the fast reaction stage during the CaO carbonation suddenly finished.[26] Thus, the initially fast stage and the subsequently slow stage were controlled by the kinetic reaction and $CO_2$ diffusion through the $CaCO_3$ product layer, respectively.[27, 28]

To better understand the fast stage during the CaO carbonation, which is particularly essential for practical applications due to the short reaction time, the critical thickness of the $CaCO_3$ product layer has been extensively studied. Barker[22] demonstrated a “critical carbonate layer thickness” of 22 nm at which the carbonation reaction rate started to be controlled by $CO_2$ diffusion limitation.

However, the estimating equation adopted in that research was confounded by the uncertainties in the carbonation model. A better understanding of pore model coupled with a carbonation pattern across CaO particles was required in this model. In order to eliminate the influences of the unquantifiable and complex morphology in natural materials, the long-duration carbonation reaction on non-porous CaO particles was carried out by Mess et al.[29] It was found that the $CaCO_3$ product layer was homogeneous and exhibited a thickness up to 2 μm under very severe carbonation conditions (850 ˚C and 1.2 MPa of $CO_2$ for 2000 min). Subsequently, Alvarez and Abanades[30] refined the model proposed by Barker[22] and suggested that before the maximum product thickness was reached, the small pores in the sorbent were completely filled. In their proposed model, a $CaCO_3$ layer was generated on the outside surface of CaO grains in the carbonation reaction and an average value of 49 nm (standard deviation is around 19%) was determined.

However, the critical thickness of the $CaCO_3$ layer has only been estimated by means of computer-aided modeling.[22, 26, 29, 30] There has been no direct observation and measurement of the critical thickness of $CaCO_3$ product layer formed in the CaO carbonation reaction. Thus, a detailed experimental study is highly desirable for the design of novel CaO adsorbents and the understanding of mechanisms of CaO carbonation.

In addition, most of the CaO carbonation work in the open literature was carried out at temperatures higher than 500 ˚C. Only limited information on low-temperature carbonation of CaO at around 400 ˚C has been reported due to the relatively low reaction rate and low capacity of carbon capture.[31, 32] We have found that there are two stages of fast CaO carbonation maximising the reaction rate at 400 and 600 ˚C, respectively. Normally, one stage of the fast carbonation reaction was reported in other work for non-isothermal CaO carbonation when the temperature was increased from room temperature to 900 ˚C.[33] However, the presence of the carbonation gap between 400 and 600 ˚C has

not been clearly understood.

Furthermore, a potentially novel intensified process combining $CO_2$ capture and utilisation at around 400 ˚C could be very interesting. For example, Duyar et al.[34] reported that using a dual-functional catalyst for $CO_2$ capture at 320 ˚C, followed by the introduction of $H_2$ at the same reaction temperature, resulted in the regeneration of sorbent and the production of methane. In this scenario, the regeneration of sorbents and the conversion of captured $CO_2$ were processed without an energy-intensive thermal-swing process. Therefore, it is of interest to understand the formation of the $CaCO_3$ layer during CaO carbonation at key reaction temperatures of 400 ˚C and 600 ˚C. In this work, two types of CaO adsorbents possessing different porosities were studied in relation to the critical thickness of $CaCO_3$ product layer.

## 2. Experimental section

### 2.1 Adsorbent preparation

A standard sol-gel process proposed by Santos et al.[35] was used to synthesise a CaO adsorbent. Predetermined amounts of calcium nitrate tetrahydrate ($Ca(NO_3)_2{\cdot}4H_2O$, Sigma-Aldrich, 99.99%) and citric acid monohydrate ($C_6H_8O_7{\cdot}H_2O$, Sigma-Aldrich, 99.99%) acting as chelation agent, were added to the distilled water at room temperature (water and citric acid to metal ion molar ratios were 40:1 and 1:1, respectively). The mixture was continuously stirred at 80 ˚C to form a translucent pale-yellow sol with good dispersion. After drying overnight at 130 ˚C of the prepared sol, the translucent pale-yellow sol turned into a low-density foam. The obtained foam was then calcined in a muffle furnace at 850 ˚C for 5 h with a heating rate of 2 ˚C $min^{-1}$. This synthesized sample was designated as sol-gel CaO. A commercial CaO (Sigma-Aldrich, 99.99%) was used as the reference adsorbent after dried overnight at 130 ˚C.

### 2.2 Carbonation/calcination tests

The carbon capture performance of adsorbents was conducted in both a fixed-bed reactor (as shown in Fig. 1) and a thermogravimetric analyser (TGA, SDT Q600). In the case of the fixed-bed test, 500 mg of adsorbent was loaded into the sample tube (6.35 mm in diameter). Both the carbonation and calcination processes were performed with a temperature-swing process with a heating rate of 10 ˚C $min^{-1}$ under 15% $CO_2$ balanced with $N_2$. The total flow rate of gases was controlled at 100 mL $min^{-1}$. The reacted CaO samples produced at both 400 ˚C and 600 ˚C in the fixed-bed reactor were denoted as sol-gel FB-400 and sol-gel FB-600 for the sol-gel CaO, and FB-400 and FB-600 for the commercial CaO, respectively. After calcination, the sample was denoted as FB-des. The same carbonation/calcination test was repeated over 3 cycles.

During the TGA test, around 15 mg of adsorbent was placed in an alumina crucible and heated to 800 ˚C with a heating rate of 20 ˚C $min^{-1}$ under the $N_2$ atmosphere (100 mL $min^{-1}$). When the temperature decreased to room temperature, further increasing the temperature to 400 ˚C, 15% $CO_2$ was used to carbonate the sample for 10 h and then increase the temperature to 600 ˚C for 30 min.

The carbonation conversion was calculated as follows:[36]

$$X(\%) = \frac{m_t - m_0}{m_0} \cdot \frac{M_{CaO}}{M_{CO_2}} \cdot 100\% \quad (1)$$

where X is the carbonation conversion, $m_0$ is the mass of the sample after calcination, $m_t$ is the mass of the sample after carbonation for t minutes, and $M_{CaO}$ and $M_{CO_2}$ are the mole masses of CaO and $CO_2$, respectively.

### 2.3 Characterisation of adsorbents

Powder X-ray diffraction (XRD) was performed on a PANalytical empyrean series 2 diffractometer with Cu Kα radiation. Data were analysed by X'pert Highscore plus software. $N_2$ adsorption-desorption isotherms were collected using an ASAP 2000 analyser at -196 ˚C. The

Brunauer-Emmett-Teller (BET) surface area was calculated using the adsorption branch data at the relative pressure ($P/P_0$) from 0.06 to 0.2, and the micropore volume ($V_{micro}$) was calculated by the t-plot method.[37] The pore size distribution was calculated by the Barrett-Joyner-Halenda (BJH) method using nitrogen desorption branch data.

The surface morphology and microstructure of samples were characterised using scanning electron microscopy (SEM, a Stereoscan 360) and transmission electron microscopy (TEM, JEOL 2010), respectively. For TEM analysis of bulky solid samples, the samples were ground, dispersed with acetone, and then deposited on a Cu grid covered with a perforated carbon membrane.

A Nanolab Dualbeam focused ion beam (FIB)-SEM coupled with an energy-dispersive X-ray spectroscopy (EDX) and TEM coupled with selected area electron diffraction patterns, were used to characterise and examine the critical thickness of the product layer deposited on the carbonated adsorbents. For FIB-SEM analysis, the samples were cut using a focused ion beam to produce small cross-section samples, which were attached to TEM grids using a platinum binder. After that, the grids with the cross-section samples were analysed using TEM.

The crystalline phase change during the carbonation process for CaO and sol-gel CaO was detected by the in-situ XRD. The Bruker D8 Advance XRD equipped with an Anton-Paar XRK-900 high-pressure XRD cell and a Cu kα source (0.154 nm) was conducted to collect the XRD patterns. Sample activation was conducted at 800 ˚C in pure $N_2$ (1 bar, 50 mL $min^{-1}$) for 60 min, with a heating rate of 10 ˚C $min^{-1}$ before cooling to 400 ˚C for data collection. The sample was pre-treated with 15% $CO_2$ balanced with $N_2$ for 60 min and XRD patterns were continuously collected with the scanning ranging from 22.5˚ to 40˚ with a step size of 0.1˚ and dwell time of 1 s (15 min scans yielding 4 patterns to observe the phase changes).

## 3. Results and discussion

### 3.1 Characterisations of adsorbents

$N_2$ adsorption-desorption isotherms and pore size distributions were conducted to determine the structure of the CaO materials (Fig. 2). The textural properties of different CaO adsorbents are summarised in Table 1. The BET surface area (38.51 $m^2$ $g^{-1}$) and total pore volume (0.1527 $cm^3$ $g^{-1}$) of the sol-gel CaO are much higher than those of the commercial CaO (20.96 $m^2$ $g^{-1}$ and 0.0314 $cm^3$ $g^{-1}$, respectively) due to the presence of micro-scale agglomerates generated by the voids between the nano-scale grains,[35] which favor $CO_2$ carbonation performance.[38, 39] The BJH pore size distribution (Fig. 2b) indicates the formation of abundant mesopores and macropores ranging from 2 to 100 nm in the sol-gel CaO. The morphologies of the commercial CaO and the sol-gel CaO are displayed in Fig. 3a and b, respectively. The commercial CaO possesses a compact structure with a smooth surface and the diameter of CaO grains ranges from 1.5 to 2 μm (Fig. S1a). Compared to the commercial CaO, the sol-gel CaO exhibits a much more fluffy and porous structure. In addition, the diameter of the sol-gel CaO grains ranges from 120 nm to 180 nm as shown in Fig. S1b. Pores less than 10 nm are observed in the commercial CaO as shown in Fig. 3g in agreement with the distribution of small pores ranging from 2 nm to 10 nm in Fig. 2b. However, mesopores composed of nano-sized grains are observed only in the sol-gel CaO, which is consistent with the BJH size distribution (Fig. 2b).

### 3.2 Carbon capture testing

The carbonation of CaO at 400 and 600 ˚C was observed using a fixed-bed reactor. As shown in Fig. 4a and b, both the commercial CaO and the sol-gel CaO exhibited a dramatic CaO conversion at 400 ˚C. However, a further increase in temperature resulted in a sudden reduction of carbonation rate at around 500 ˚C for both samples. The carbonation rate of the CaO increased again when the

temperature reached 600 ˚C. However, as shown in Table 2, the $CO_2$ uptake, from the 1st cycle to the 2nd cycle, declined dramatically at a carbonation temperature of around 400 ˚C for both the commercial CaO and the sol-gel CaO, while only a slight decrease of $CO_2$ uptake is observed after carbonation at 600 ˚C. Compared to the 2nd cycle performance of $CO_2$ capture, the 3rd cycle carbon capture exhibited slightly decreased carbonation rates at both 400˚C and 600 ˚C. It is noted that all characterizations of materials are from 1st cycle carbon capture. It is suggested that with the increase of carbonation/calcination cycles, less effect was observed on the carbon capture performance at the second carbonation stage at around 600 ˚C. A more detailed understanding of mechanisms in relation to the increase of carbonation/calcination cycles is suggested for future.

In order to eliminate the influence of moisture and other impurities inside the sorbent, both the commercial CaO and the sol-gel CaO samples were heated to 800 ˚C under $N_2$ atmosphere; then the samples were cooled to 400 ˚C for the $CO_2$ capture stage. Fig. S2 shows that the weight of the CaO sample was increased initially due to the carbonation reaction and then showed relative stability at 400 ˚C, indicating that carbonation of CaO was almost completed at 400 ˚C. In addition, the sample was held at 400 ˚C for 10 h prior to heating it to 600 ˚C for further carbonation. This is to ensure that CaO carbonation at 600 ˚C was not due to incomplete carbonation at 400 ˚C. As shown in Fig. S2, carbonation is clearly observed at 600 ˚C indicating the presence of a true two-stage fast carbonation of CaO at around 400 and 600 ˚C, respectively.

A few studies have reported the existence of a reaction rate gap in the CaO carbonation when the temperature ranges from 400 to 600 ˚C. Bhatia and Perlmutter[40] proposed that when the temperature was lower than 515 ˚C, the CaO carbonation reaction as shown in Eq. (2) and (3) took place on the pore surface and was governed by the diffusion of $CO_2$ molecules with an activation energy of 88.9 $\pm$3.7 kJ $mol^{-1}$. The ionic diffusion process is shown in Fig. S3a. This is consistent with the

observation of CaO carbonation at around 400 ˚C in this work. However, increasing the temperature of CaO carbonation to higher than 515 ˚C, the reaction was reported to take place at the interface between CaO and $CaCO_3$ as described in Eq. (4), where $CO_3^{2-}$ is the diffusion species with an activation energy about 179.2±7.0 kJ $mol^{-1}$ [40] as shown in Fig. S3b.

T<515 ˚C, carbonation occurs at the pore surface:

$$CO_2\ (g) \rightleftharpoons (CO_2)_{ads} \quad (2)$$

$$(CO_2)_{ads} + O^{2-} \rightarrow CO_3^{2-} \quad (3)$$

T>515 ˚C, carbonation occurs at the CaO-$CaCO_3$ interface:

$$CO_3^{2-} + CaO \rightarrow CaCO_3 + O^{2-} \quad (4)$$

**3.3 Mechanisms of CaO carbonation**

XRD results for the CaO samples are shown in Fig. 5. For the fresh commercial CaO and sol-gel CaO samples, only one CaO phase is observed. After carbonation at 400 ˚C, the spent adsorbents exhibit a weak diffraction peak at 2θ=29.4˚, indicating the characteristic peak of $CaCO_3$ (1 0 4).[41] The XRD patterns for the commercial CaO and the sol-gel CaO after carbonation at 600 ˚C exhibit much stronger diffraction peaks at similar positions. This indicates that more $CaCO_3$ phases were generated at 600 ˚C compared with the reacted CaO sorbents obtained at 400 ˚C. The diffraction peaks of $CaCO_3$ disappear after increasing the carbonation temperature to 800 ˚C. This is attributed to the decomposition of $CaCO_3$ at 800 ˚C.

After carbonation of the commercial CaO and the sol-gel CaO at 400 and 600 ˚C, similar morphologies are observed for both FB-400 and FB-600 (Fig. 3c and e). From Fig. 3d and f, the mesopores in the sol-gel CaO appear to diminish after carbonation at 400 and 600 ˚C. Nevertheless, there are many attachments on the surface of the sol-gel CaO carbonated at 400 ˚C observed in the SEM images (Fig. 3d), showing that the mesopores between small grains are well connected.

However, the sol-gel CaO experienced a dramatic decrease of pores and the growth of grains after carbonation at 600 ˚C due to the volume increase of the sorbent, as shown in Fig. 3f.

FIB-SEM coupled with EDX was used to measure the critical thickness of the $CaCO_3$ product layer as shown in Fig. 6. It is noted that the top layer observed in the cross-section was coated with indium which was used to protect the surface during the cutting of the CaO samples.[42] As for the commercial CaO, no product layer can be observed after carbonation at 400 ˚C as shown in Fig. 6a. However, a uniform distribution of carbon element is shown in EDX mapping (Fig. S4) implying that $CaCO_3$ was formed uniformly within the commercial CaO during carbonation at 400 ˚C. The existence of $CaCO_3$ is also confirmed from the XRD analysis of FB-400 (Fig. 5a). The commercial CaO sample has a bulk particle size around 3 mm with small grains (around 1.5 μm) containing small pores ranging from 2 nm to 10 nm.[43, 44] It appears that carbonation of the commercial CaO at 400 ˚C is dominated by the kinetic reaction between CaO and $CO_2$, and the small pores in the grains were filled with the $CaCO_3$ formed. Although a layer of $CaCO_3$ is not observed on the FB-400 sample, EDX analysis (Fig. 7a and b) shows that the concentration of carbon in relation to $CaCO_3$ inside the small grains of the commercial CaO was around 5.44%, which is lower than the concentration of carbon on the surface of the commercial CaO (6.16%) (FB-400). This indicates that the outer layer of the CaO was concentrated with $CaCO_3$ in the fast carbonation stage at 400 ˚C. A distinct layer is observed after the CaO sample was carbonated at 600 ˚C. It is suggested that after the carbonation, the internal pores in the grain have been filled and a layer of product was formed on the outside of the grain. It can be seen from Fig. S5 that the average thickness of the product ($CaCO_3$) is around 90 nm. It is noted that the FB-600 sample was obtained when the maximum carbonation rate was reached during carbonation at 600 ˚C in the fixed-bed reactor. In addition, the distributions of oxygen and carbon elements show a gradual increase from the interior to the surface

of the CaO grains as shown in the EDX mapping of the FB-600 (Fig. 6f and g). By contrast, the weight percentage of calcium exhibits a decrease from the inner grains to the surface of the FB-600 CaO. Similar results are observed in Fig. 7c and d. The weight percentage of carbon on the surface of the commercial CaO grains (5.96%) is twice as much as in the interior of the CaO grains (2.99%). This phenomenon suggests that the carbonation reaction happened on the interface between CaO and $CaCO_3$. $CO_2$ diffuses through the $CaCO_3$ layer as $CO_3^{2-}$ ions.[40] Therefore, the concentration of carbon elements corresponding to $CO_3^{2-}$ ions is higher on the surface of CaO grains after carbonation at 600 ˚C, compared to the carbon concentration inside the CaO grains.

In this stage, $CO_3^{2-}$ ions can decompose to produce $CO_2$ and $O^{2-}$ as shown in Eq. (4). $CO_2$ molecule transfers to a neighboring, similarly vacated site, while $CO_2$ produced elsewhere moves to take its place and reform the $CO_3^{2-}$. Therefore, the $CO_2$ molecule diffuses from site to site through the $CaCO_3$ product layer, until ultimately the carbonation reaction occurs at the interface between CaO and $CaCO_3$. The ionic diffusion process is shown in Fig. S3b. A higher activation energy, about $179.2 \pm 7.0$ kJ $mol^{-1}$, is required for the decomposition of $CO_3^{2-}$. This activation energy corresponds to a carbonation temperature around 600 ˚C, where the second-stage fast CaO carbonation occurred. The sudden change in activation energy between 500 and 600 ˚C could also be due to the phase change of $CaCO_3$ from aragonite to calcite.[45] The diffusion of ions within aragonite is much easier than calcite. The diffusion of ions (e.g., $CO_3^{2-}$) is related to Tammann temperature (which is half the absolute melting point, and the temperature at which bulk diffusion starts to become significant), which is around 412 ˚C for aragonite and around 650 ˚C for calcite. In-situ XRD analysis of CaO carbonation at a temperature of 750 ˚C has been investigated and, to date, only calcite was reported [46]. However, at a lower carbonation temperature of 450 ˚C, aragonite-type $CaCO_3$ appears to be formed, according to in-situ XRD experimental tests.[47]

In this work, the phase changes in the carbonation reaction at different temperatures were investigated using an in-situ XRD equipment, as shown in Fig. 8. It is found that calcite was the only phase of $CaCO_3$ observed with the increase of both the reaction time and temperature. Therefore, the sudden change of CaO carbonation is unlikely due to the phase change of $CaCO_3$ from aragonite to calcite during the carbonation of CaO samples. However, a high-resolution synchrotron XRD could be used to further confirm the absence of aragonite during CaO carbonation, which might exist as an intermediate product.

In order to understand the influence of temperature on the critical thickness of the product layer during the fast CaO carbonation, FIB-TEM coupled with selected-area electron diffraction patterns were produced, as shown in Fig. 9. Even though no $CaCO_3$ product layer was observed in Fig. 9A, (012) and (104) crystal phases of $CaCO_3$ were observed in the electron diffraction pattern (Fig. 9a) which is in agreement with XRD results in Fig. 5a. In addition, (001) crystal phase ($Ca(OH)_2$) was observed due to the reaction between the thin FIB-TEM sample (around 100 nm) and moisture in the air. Three distinct layers and single-crystal characteristics after the carbonation at 600 ˚C are shown in Fig. 9B and Fig. 9b, respectively. The outside layer was caused by the coating of indium and platinum. The compact layer in the middle was the formed $CaCO_3$ product layer, with a thickness around 90 nm. This phenomenon indicates that, as with commercial CaO, carbonation at 400 ˚C and 600 ˚C involves filling $CaCO_3$ in the small pores in the grains, and a product layer deposited on the outside of the grains, respectively.

**3.4 Influence of porous structure**

Abundant mesopores, ranging from 2 to 100 nm, were generated by the lamellar structure in the sol-gel CaO (Fig. 3b), which enhance the fast and kinetically-limited reaction stage. In addition, large pore volume favors gas diffusion in the pore space of adsorbents.[48] Therefore, the sol-gel CaO

performed a higher carbon capture capacity compared to the commercial CaO in Table 2. No obvious product layer was observed in the sol-gel CaO after carbonation at both 400 ˚C and 600 ˚C, as shown in Fig. 6c and d. The distribution of carbon is consistent between the surface and the inner grains of the sol-gel CaO grains (Fig. 7e and f). It appears that the carbonation of sol-gel CaO at 400 ˚C is similar to that of commercial CaO, involving the filling of small pores in the CaO grains with the formed $CaCO_3$. However, the carbonation at 600 ˚C is retarded by the lack of useful porosity (the confinement effect) which is required for the growth of $CaCO_3$ instead of the formation of $CaCO_3$ product layer, as shown in Fig. 10b.[44] This is attributed to that local space is required for the growth of particles from 16.7 to 36.9 $cm^3$ $mol^{-1}$ for the conversion of CaO to $CaCO_3$. The FIB-TEM image of sol-gel FB-600 as shown in Fig. 9C exhibits almost no porosity which is good agreement with the FIB-SEM pictures in Fig. 6d. In addition, the crystal phases ($CaCO_3$ and $Ca(OH)_2$) were observed in Fig. 9c, further indicating the formation of $CaCO_3$ in the sol-gel FB-600. Therefore, fabricating nano-CaO having dimensions less than the critical thickness of the $CaCO_3$ layer (~90 nm) is of potentially great significance if it can be done cheaply and in bulk. For example, nanowire and nanofilm of the novel nano-CaO could be developed. However, the resistance of sorbent sintering during the process of carbonation/calcination remains a challenging topic. Furthermore, it is suggested to disperse CaO species into an inert support which can provide a certain extent of porosity, prohibit CaO sintering and play an essential role in restricting the growth of $CaCO_3$ layer.

## 4. Conclusions

The formation of $CaCO_3$ product layer on the outside surface of CaO grains during the fast reaction stage for carbon capture using two types of CaO has been systematically studied. It was found that

for both the commercial CaO and the sol-gel CaO, two distinct stages of fast carbonation are observed at 400 and 600 ˚C. After carbonation at 600 ˚C for the commercial CaO, a layer of $CaCO_3$ with a thickness around 90 nm is observed. This is because the internal pores of the commercial CaO grains have been filled with $CaCO_3$ and a layer of the $CaCO_3$ product is deposited on the outside of the CaO grain. Here, the fast carbonation stage of the commercial CaO is terminated by the formation of the $CaCO_3$ layer. However, as with the synthesized sol-gel CaO, the carbonation reaction is retarded by the lack of useful porosity (space is required for the formation of CaCO3 due to its larger molar volume than CaO), defined here as the confinement effect, instead of by the formation of a $CaCO_3$ product layer itself. Thus, a layer of $CaCO_3$ product on the sol-gel CaO cannot be observed after carbonation at 600 ˚C. This is attributed to the presence of abundant mesopores generated by the lamellar structure of the sol-gel CaO.

## Conflicts of interest

There are no conflicts to declare.

## Acknowledgements

The authors are grateful for the financial support of the National Natural Science Foundation of China (no. 21706050) and China Scholarship Council (CSC, no. 201606450016).

## References

1. R. Han, J. Gao, S. Wei, Y. Su and Y. Qin, *J. Mater. Chem. A*, 2018, **6**, 3462-3470.

2. *Climate change 2014-impacts, adaptation and vulnerability: regional aspects*, Intergovernmental Panel on Climate Change, 2014.

3. W. Obergassel, C. Arens, L. Hermwille, N. Kreibich, F. Mersmann, H. E. Ott and H. WangHelmreich, *Environmental Law and Management*, 2016, **28**, 3-12.

4. F. Yan, J. Jiang, M. Zhao, S. Tian, K. Li and T. Li, *J. Mater. Chem. A*, 2015, **3**, 7966-7973.

5. H. Sun, J. Wang, J. Zhao, B. Shen, J. Shi, J. Huang and C. Wu, *Appl. Catal. B: Environ.*, 2019, **244**, 63-75.

6. R. S. Haszeldine, *Science*, 2009, **325**, 1647-1652.

7. M. M. Sadiq, H. Li, A. J. Hill, P. Falcaro, M. R. Hill and K. Suzuki, *Chem. Mater.*, 2016, **28**, 6219-6226.

8. Z. Sun, M. H. Sedghkerdar, J. Saayman, N. Mahinpey, N. Ellis, D. Zhao and S. Kaliaguine, *J. Mater. Chem. A*, 2014, **2**, 16577-16588.

9. F. Wang and J. Chiou, *Energ. Convers. Manage.*, 2004, **45**, 15-26.

10. P. Zhao, J. Sun, Y. Li, K. Wang, Z. Yin, Z. Zhou and Z. Su, *Energy Fuels*, 2016, **30**, 7543-7550.

11. D. P. Hanak, E. J. Anthony and V. Manovic, *Energ. Environ. Sci.*, 2015, **8**, 2199-2249.

12. G. Melaet, W. T. Ralston, C. S. Li, S. Alayoglu, K. An, N. Musselwhite, B. Kalkan and G. A. Somorjai, *J. Am. Chem. Soc.*, 2014, **136**, 2260-2263.

13. Y. A. Daza, R. A. Kent, M. M. Yung and J. N. Kuhn, *Ind. Eng. Chem. Res.*, 2014, **53**, 5828-5837.

14. H. Sun, C. M. Parlett, M. A. Isaacs, X. Liu, G. Adwek, J. Wang, B. Shen, J. Huang and C. Wu, *Fuel*, 2019, **235**, 1070-1076.

15. J. Hilz, M. Helbig, M. Haaf, A. Daikeler, J. Ströhle and B. Epple, *Fuel*, 2017, **210**, 892-899.

16. B. Arias, M. Diego, J. Abanades, M. Lorenzo, L. Diaz, D. Martínez, J. Alvarez and A. Sánchez-Biezma, *Int. J. Greenh. Gas Con.*, 2013, **18**, 237-245.

17. M. Chang, W. Chen, C. Huang, W. Liu, Y. Chou, W. Chang, W. Chen, J. Cheng, K. Huang and H. Hsu, *Energy Procedia*, 2014, **63**, 2100-2108.

18. P. Sun, J. Grace, C. Lim and E. Anthony, *AIChE J.*, 2007, **53**, 2432-2442.

19. I. Yanase, T. Maeda and H. Kobayashi, *Chem. Eng. J.*, 2017, **327**, 548-554.

20. A. I. Lysikov, A. N. S. And and A. G. Okunev, *Ind. Eng. Chem. Res.*, 2007, **46**, 4633-4638.

21. S. Choi, J. H. Drese and C. W. Jones, *ChemSusChem*, 2009, **2**, 796-854.

22. R. Barker, *J. Appl. Chem. Biotech.*, 1973, **23**, 733-742.

23. H. Sun, C. Wu, B. Shen, X. Zhang, Y. Zhang and J. Huang, *Mater. Today Sustain.*, 2018, **1**, 1-27.

24. A. Kierzkowska, R. Pacciani and C. Müller, *ChemSusChem*, 2013, **6**, 1130-1148.

25. F. Campbell, A. Hills and A. Paulin, *Chem. Eng. Sci.*, 1970, **25**, 929-942.

26. B. Arias, J. Abanades and G. S. Grasa, *Chem. Eng. J.*, 2011, **167**, 255-261.

27. J. M. Valverde, *J. Mater. Chem. A*, 2013, **1**, 447-468.

28. F. Liu, W. Li, B. Liu and R. Li, *J. Mater. Chem. A*, 2013, **1**, 8037-8044.

29. D. Mess, A. F. Sarofim and J. P. Longwell, *Energy Fuels*, 1999, **13**, 999-1005.

30. D. Alvarez and J. C. Abanades, *Ind. Eng. Chem. Res.*, 2005, **44**, 5608-5615.

31. V. Nikulshina, M. E. Galvez and A. Steinfeld, *Chem. Eng. J.*, 2007, **129**, 75-83.

32. G. MontesHernandez, R. Chiriac, F. Toche and F. Renard, *Int. J. Greenh. Gas Con.*, 2012, **11**, 172-180.

33. H. Gupta and L. Fan, *Ind. Eng. Chem. Res.*, 2002, **41**, 4035-4042.

34. M. S. Duyar, M. A. A. Trevino and R. J. Farrauto, *Appl. Catal. B: Environ.*, 2015, **168**, 370-376.

35. E. Santos, C. Alfonsín, A. Chambel, A. Fernandes, A. S. Dias, C. Pinheiro and M. Ribeiro, *Fuel*, 2012, **94**, 624-628.

36. Y. Hu, W. Liu, J. Sun, X. Yang, Z. Zhou, Y. Zhang and M. Xu, *Energy Fuels*, 2016, **30**, 6606-6613.

37. B. C. Lippens and J. De Boer, *J. Catal.*, 1965, **4**, 319-323.

38. C. Luo, Y. Zheng, C. Zheng, J. Yin, C. Qin and B. Feng, *Int. J. Greenh. Gas Con.*, 2013, **12**, 193-199.

39. M. Broda, A. M. Kierzkowska and C. R. Müller, *ChemSusChem*, 2012, **5**, 411-418.

40. S. Bhatia and D. Perlmutter, *AIChE J*, 1983, **29**, 79-86.

41. H. Zhu, Z. Liu, Y. Wang, D. Kong, X. Yuan and Z. Xie, *Chem. Mater.*, 2007, **20**, 1134-1139.

42. C. Wu and P. T. Williams, *Appl. Catal. B: Environ.*, 2010, **96**, 198-207.

43. J. Dennis and R. Pacciani, *Chem. Eng. Sci.*, 2009, **64**, 2147-2157.

44. J. C. Abanades and D. Alvarez, *Energy Fuels*, 2003, **17**, 308-315.

45. A. Lucas, M. Mouallem-Bahout, C. Carel, J. Gaudé and M. Matecki, *J. Solid State Chem.*, 1999, **146**, 73-78.

46. W. Liu, J. S. Dennis, D. S. Sultan, S. A. Redfern and S. A. Scott, *Chem. Eng. Sci.*, 2012, **69**, 644-658.

47. A. Biasin, C. U. Segre, G. Salviulo, F. Zorzi and M. Strumendo, *Chem. Eng. Sci.*, 2015, **127**, 13-24.

48. Y. Kong, G. Jiang, M. Fan, X. Shen, S. Cui and A. G. Russell, *Chem. Commun.*, 2014, **50**, 12158-12161.

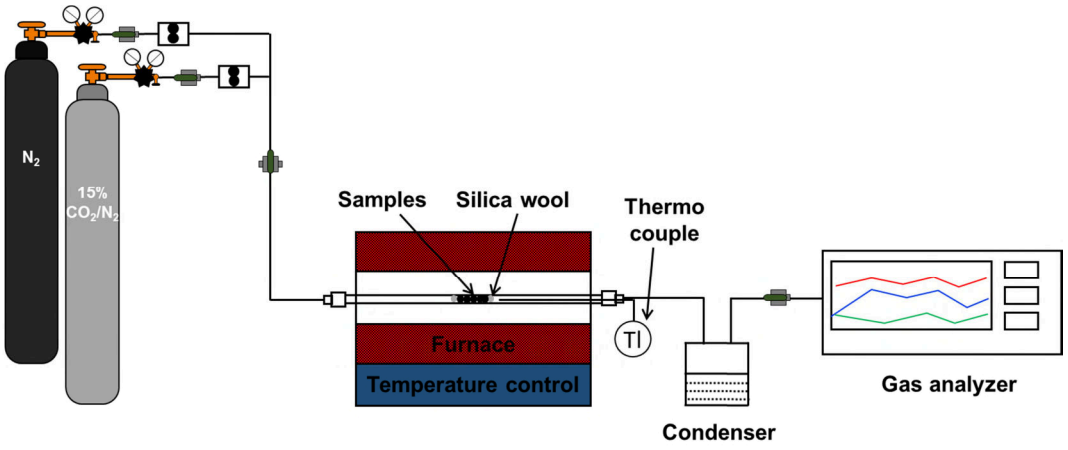


**Fig. 1** Schematic diagram of the atmospheric carbonation/calcination reactor system (fixed bed).

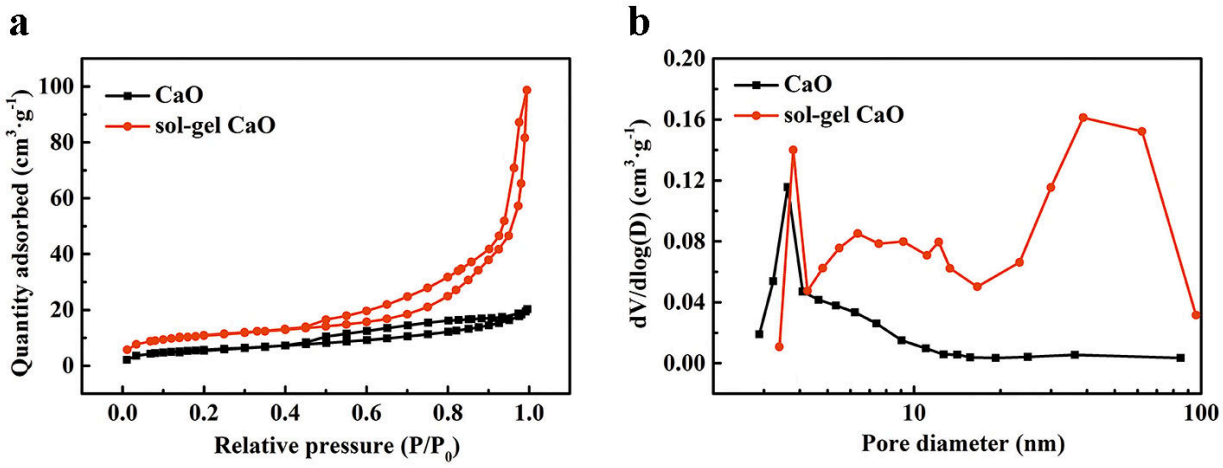


**Fig. 2** $N_2$ adsorption-desorption isotherms (a) and pore size distributions calculated from the BJH desorption branch (b).

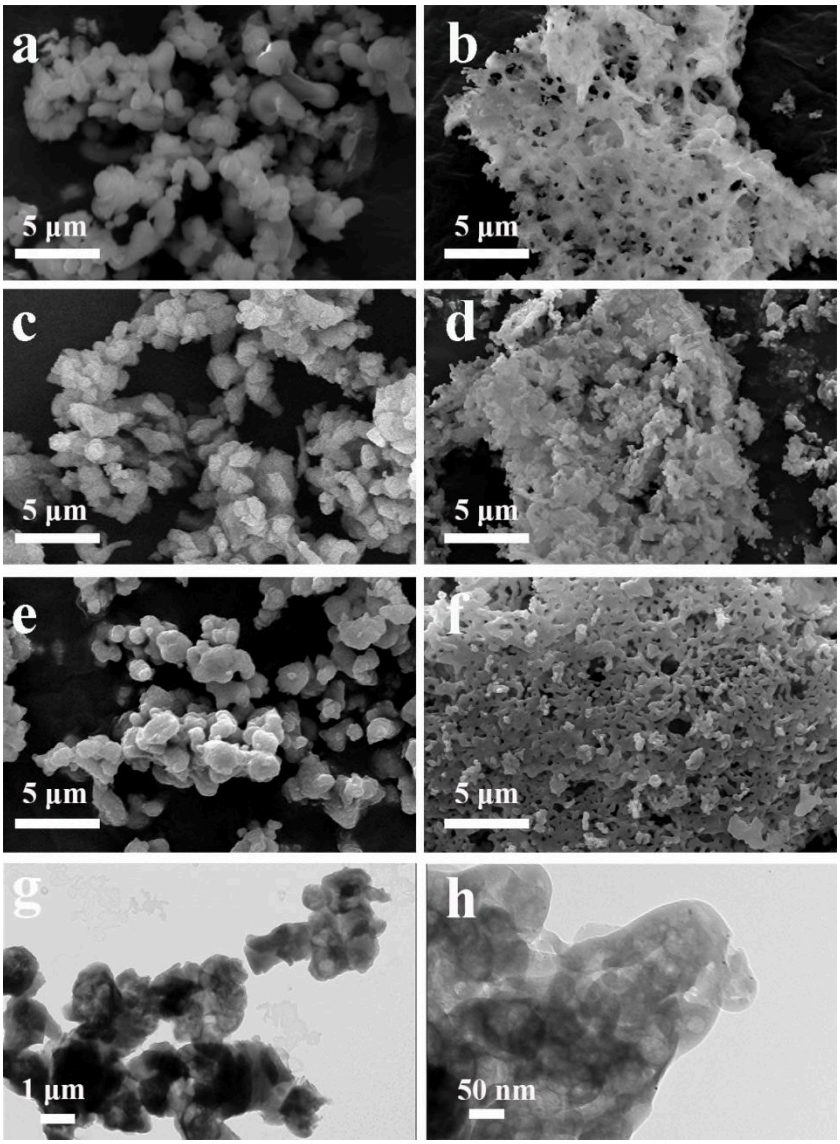


**Fig. 3** SEM images of a) CaO, b) sol-gel CaO, c) FB-400, d) sol-gel FB-400, e) FB-600, f) sol-gel FB-600 and TEM images of g) CaO, h) sol-gel CaO.

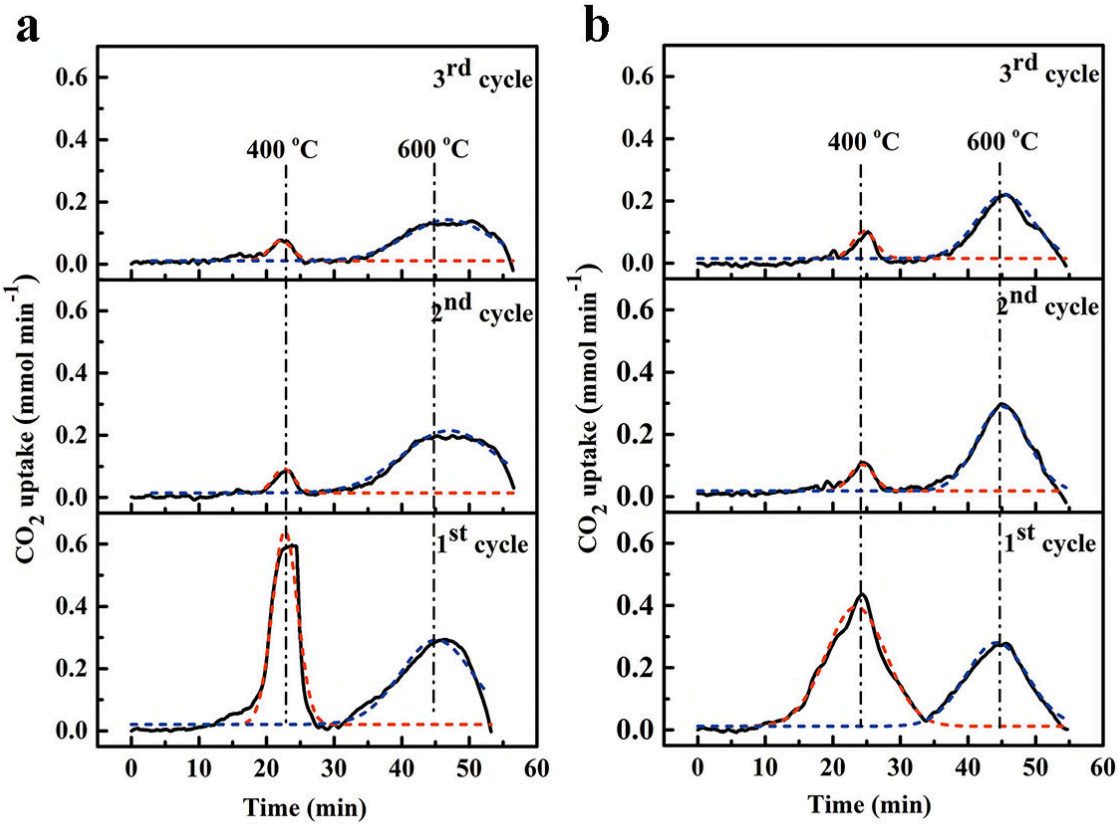


**Fig. 4** Cyclic $CO_2$ capture performance of a) CaO, b) sol-gel CaO, in a fixed-bed reactor (black line: experimental curves; red dashed curve: peak I, carbonation at 400 ˚C, blue dashed curve: peak II, carbonation at 600 ˚C).

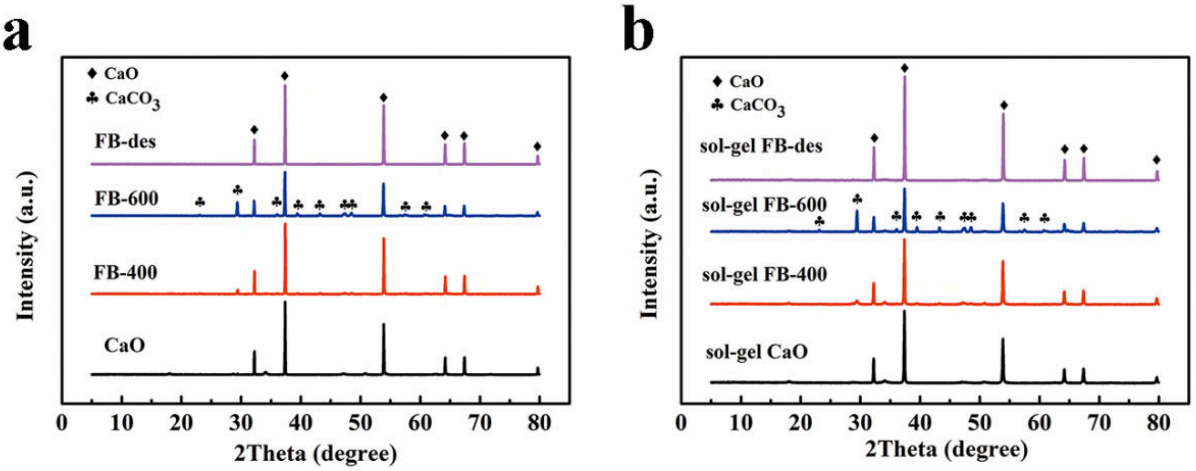


**Fig. 5** XRD patterns for CaO adsorbents obtained after reaching highest reaction rate at different temperatures. a) CaO, b) sol-gel CaO.

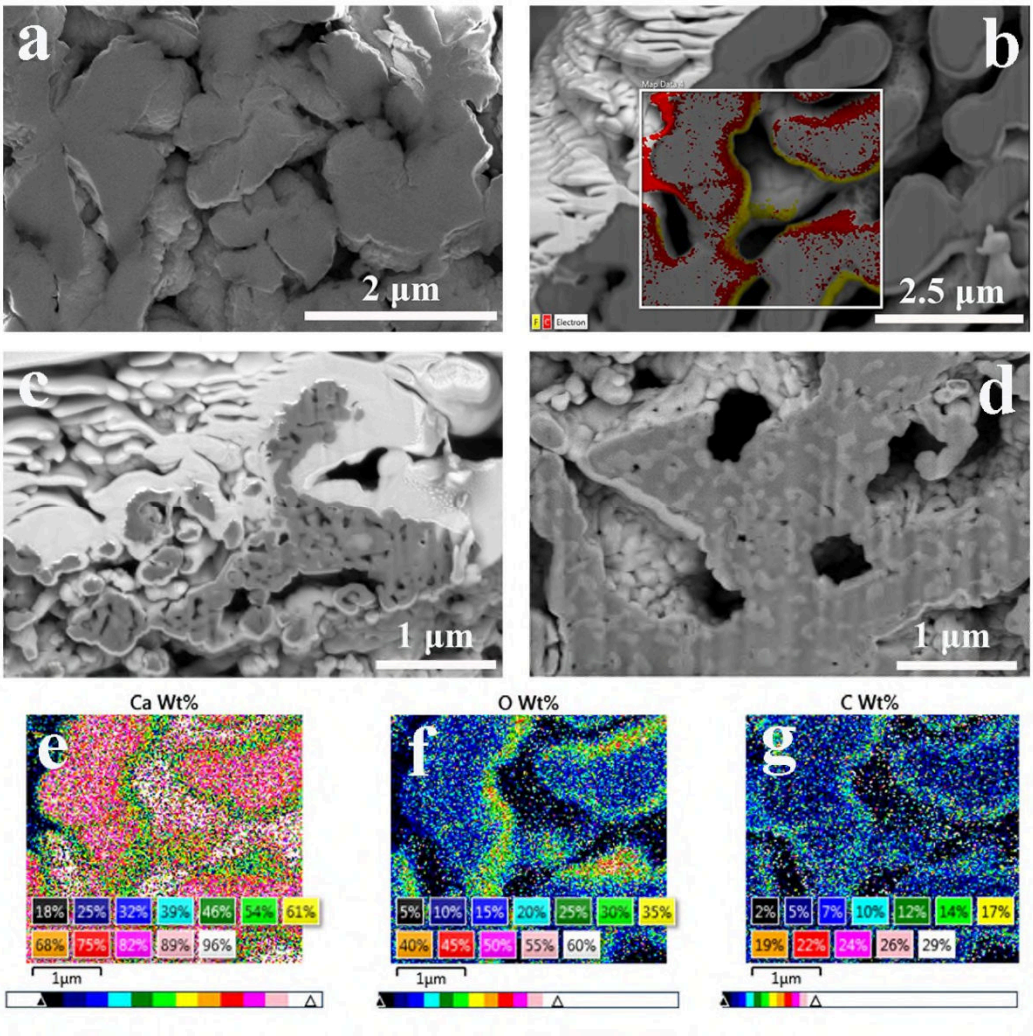


**Fig. 6** FIB-SEM images coupled with EDX mapping of the cross-section product layer. a) FB-400, b) FB-600, c) sol-gel FB-400, d) sol-gel FB-600, e) Ca element mapping, f) O element mapping, g) C element mapping.

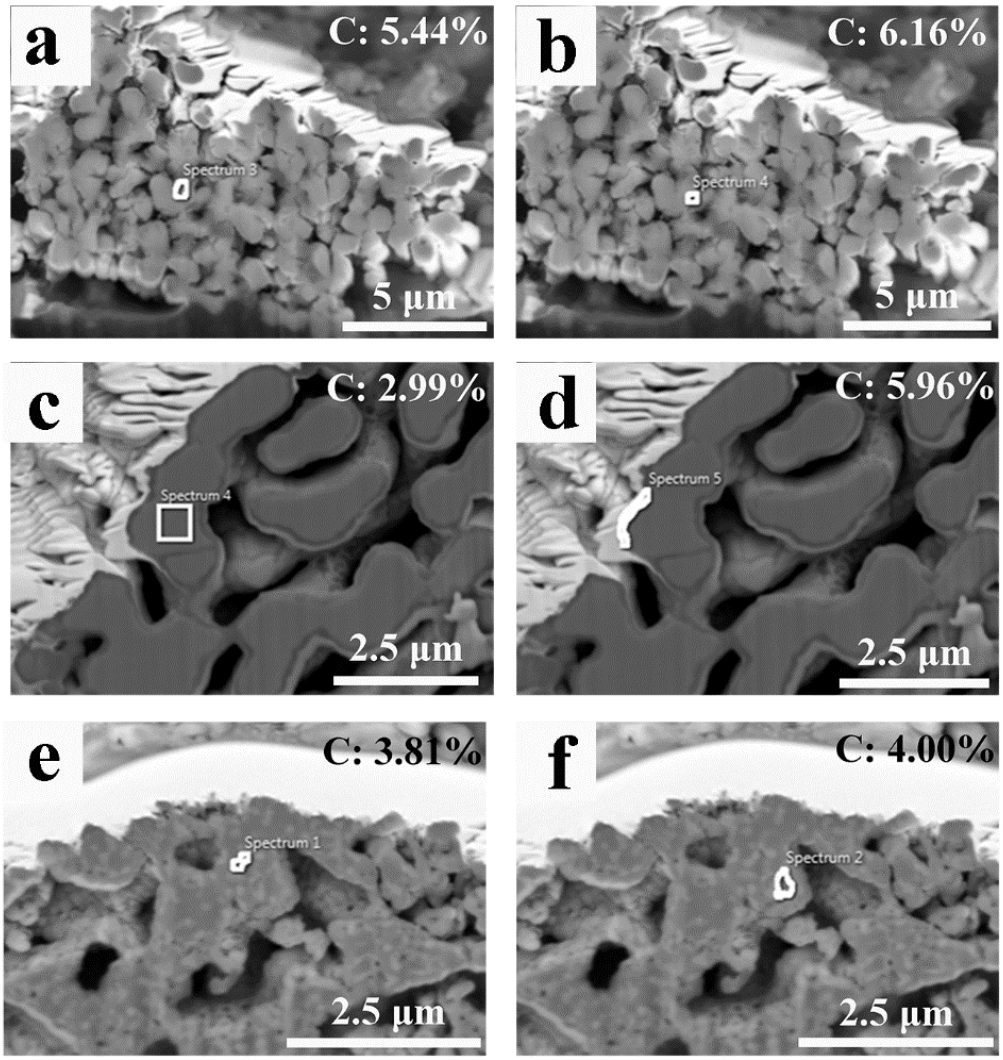


**Fig. 7** FIB-SEM images and carbon element percentage of a and b) FB-400, c and d) FB-600, and e and f) sol-gel FB-600.

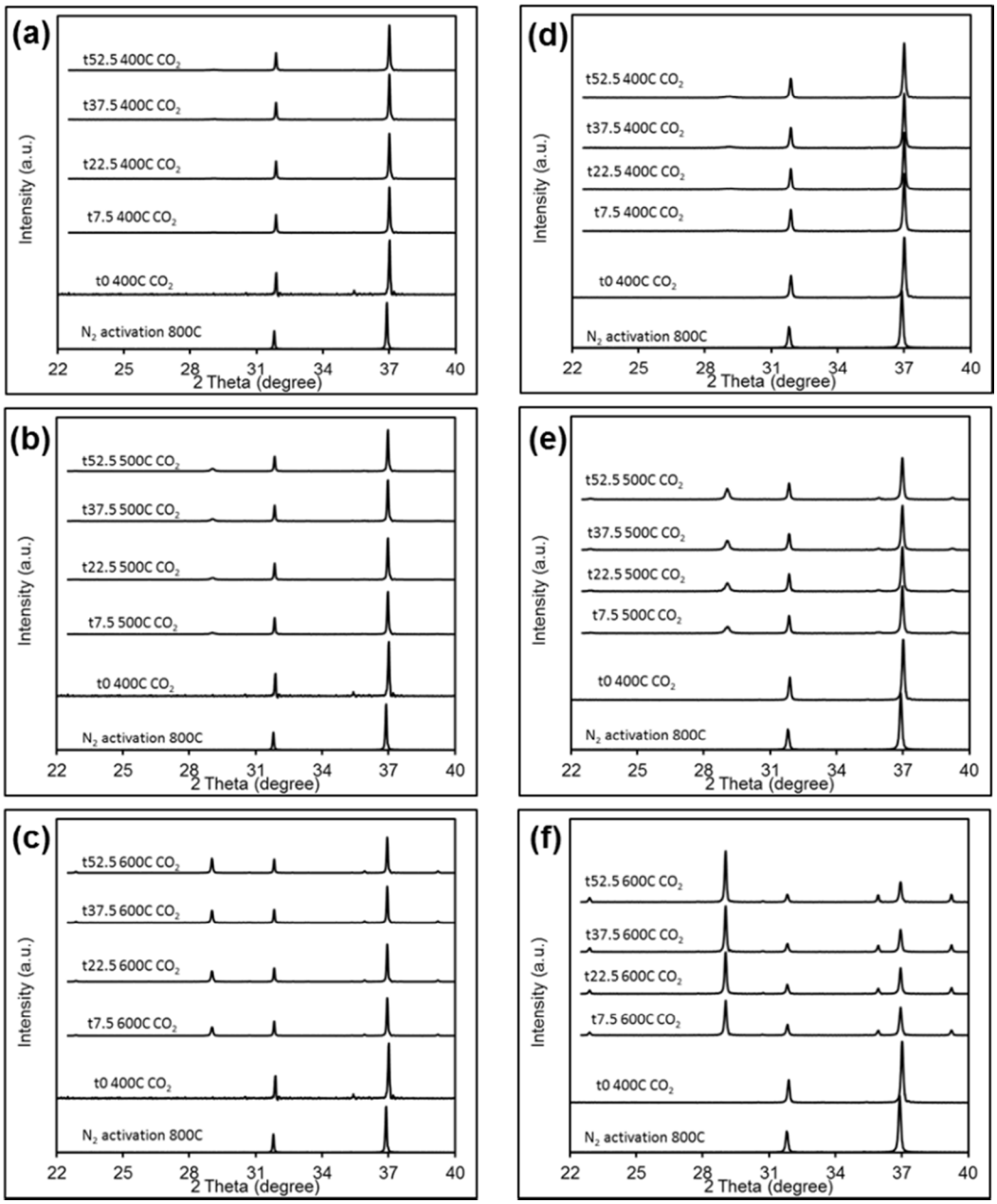


**Fig. 8** In-situ XRD patterns of CaO adsorbents at different temperatures. a) CaO 400 ˚C, b) CaO 500 ˚C, c) CaO 600 ˚C, d) sol-gel CaO 400 ˚C, e) sol-gel CaO 500 ˚C, f) sol-gel CaO 600 ˚C (txy.z represents carbonation for xy.z min).

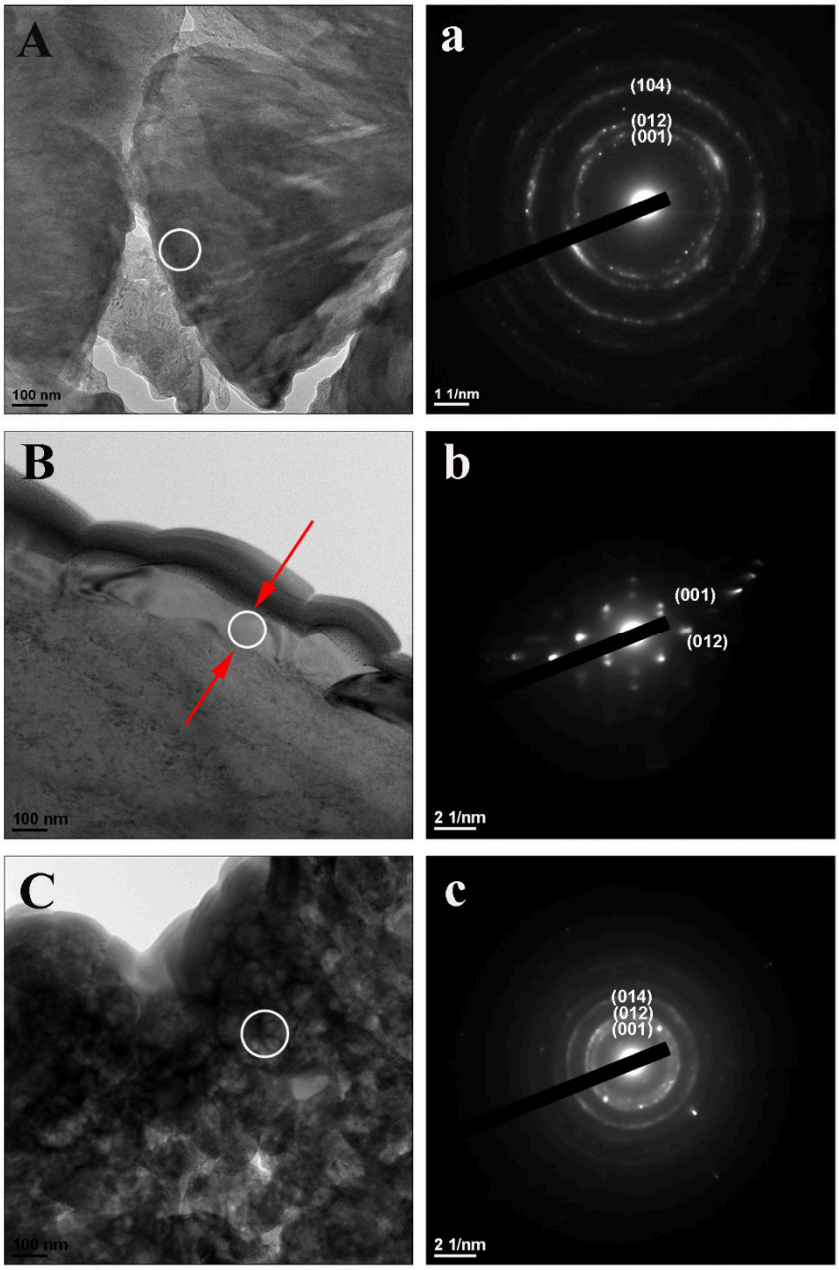


**Fig. 9** FIB-TEM images and selected-area electron diffraction pattern of the cross-section product layer. A and a) FB-400, B and b) FB-600, C and c) sol-gel FB-600.

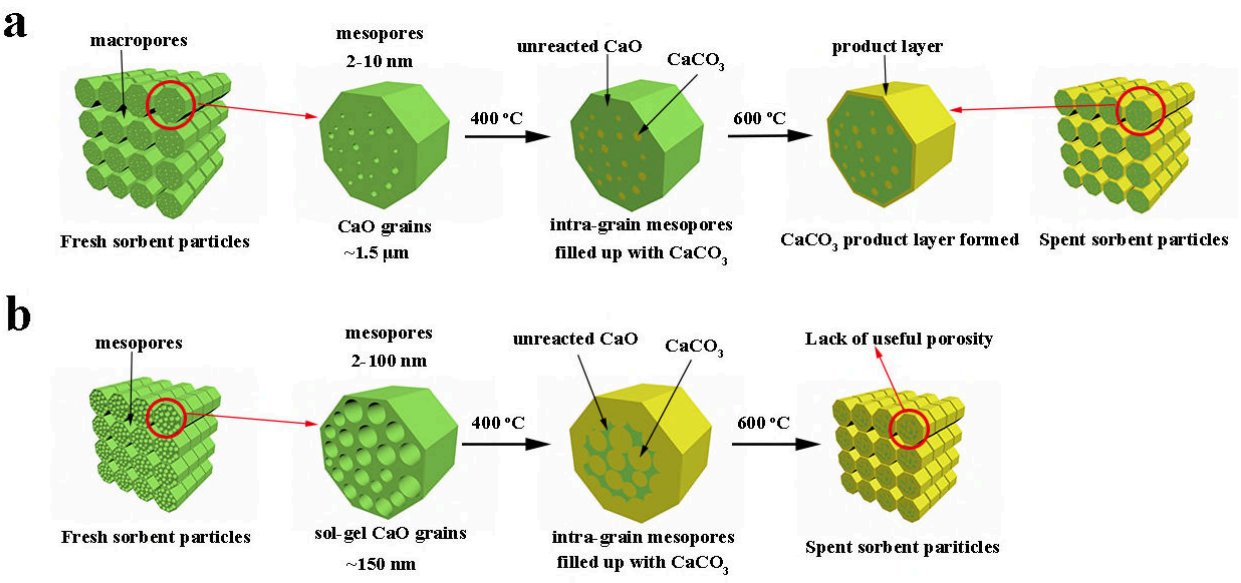


**Fig. 10** Schematic illustration of the effect of temperature and structure on the $CaCO_3$ layer thickness during CaO carbonation reaction. a) CaO, b) sol-gel CaO.

**Table 1** Textural properties derived from different CaO adsorbents

| Samples | $S_{BET}$[a] ($m^2\ g^{-1}$) | $S_{micro}$[b] ($m^2\ g^{-1}$) | $S_{meso}$[c] ($m^2\ g^{-1}$) | $V_p$[d] ($cm^3\ g^{-1}$) | $V_{micro}$[e] ($cm^3\ g^{-1}$) | $V_{meso}$[f] ($cm^3\ g^{-1}$) |
|---|---|---|---|---|---|---|
| **CaO** | 20.96 | 3.70 | 17.26 | 0.0314 | 0.0014 | 0.0331 |
| **sol-gel CaO** | 38.51 | 8.51 | 30.00 | 0.1527 | 0.0035 | 0.1511 |

[a]BET surface areas

[b]Micropore surface areas calculated by t-plot method

[c]Mesopore surface areas equal to $S_{BET}$ minus $S_{micro}$

[d]Total pore volume measured at a relative pressure ($P/P_0$) of 0.99

[e]The t-plot micropore volume

[f]BJH adsorption cumulative volume

**Table 2** $CO_2$ uptake of a commercial CaO and a sol-gel CaO at different temperatures in a fixed-bed reactor

| $CO_2$ uptake | 1st cycle | | 2nd cycle | | 3rd cycle | |
|---|---|---|---|---|---|---|
| ($mmol\ g^{-1}$) | 400 ˚C | 600 ˚C | 400 ˚C | 600 ˚C | 400 ˚C | 600 ˚C |
| CaO | 5.84 | 7.26 | 0.60 | 7.02 | 0.54 | 4.06 |
| sol-gel CaO | 8.50 | 6.16 | 0.76 | 5.12 | 0.74 | 4.20 |